2D-3D hetero-structured butylammonium-Cs-formamidinium lead trihalide perovskites for stable and efficient solar cells

Zhiping Wang, Qianqian Lin, Francis P. Chmiel, Nobuya Sakai, Laura M. Herz, Henry J. Snaith*

Clarendon Laboratory, Department of Physics, University of Oxford, Parks Road, Oxford, OX1 3PU, United Kingdom

**Correspondence: Prof. Henry J. Snaith, henry.snaith@physics.ox.ac.uk*

Abstract

Three-dimensional (3D) organic-inorganic perovskite solar cells have undergone a meteoric rise in cell efficiency to > 22%. However, the perovskite absorber layer is prone to degradation in water, oxygen and UV light. Two-dimensional (2D) Ruddlesden–Popper layered perovskites have exhibited promising environmental stability, but perform less well in solar cells, possibly due to the inhibition of out-of-plane charge transport by the insulating spacer cations. Alternatively, moving away from methylammonium, to the mixed cation formamidinium-caesium based perovskites has led to considerably enhancement of the stability of 3D perovskite absorber layers. Here, we report highly efficient and stable perovskite solar cells based on a self-assembled butylammonium-Cs-formamidinium mixed-cation lead mixed-halide perovskite photoactive layer. Long-chain alkyl-ammonium halides added to the formamidinium-cesium based perovskite precursor solution strongly enhances the crystallinity of the 3D perovskite phase, while also inducing the formation of new layered-phases in the films. By carefully regulating the composition, we are able to achieve “plate-like” layered perovskite crystallites standing up between the host 3D perovskite grains. This spontaneously forming heterostructure allows the efficient charge carrier transport in the 3D perovskite phase, while reducing charge recombination via fortuitous grain boundary passivation. We also observe reduced current-voltage hysteresis and improved device stability, which we correlate to enhanced crystallinity and reduced crystal defects in the 3D perovskite phase. With the optimized composition, we achieved a power conversion efficiency of 20.6% (stabilised efficiency of 19.5%) from a narrow bandgap (1.61 eV) perovskite solar cell and of 17.2 % (stabilised efficiency of 17.3%) from a wider bandgap (1.72 eV) perovskite solar cell optimised for tandem applications. In addition to enhanced efficiency, the addition of butylammonium greatly enhances the long-term stability of the devices. For the first time, our cells sustain more than 80% of their “post burn-in” efficiency after 1,000 hrs

of aging under simulated full spectrum sun light measured in an ambient environment without encapsulation. With additional sealing with a glass/polymer-foil/glass laminate, we extend this lifetime to close to 4,000 hrs. Our work illustrates that engineering heterostructures between 2D and 3D perovskite phases is both possible, and can lead to enhancement of both performance and stability of perovskite solar cells.

Introduction

Organic-inorganic metal halide perovskites have emerged as one of the most promising next-generation photovoltaic materials thanks to their eminent properties, such as tunable band gap[1,2], long electron-hole diffusion lengths[3], low recombination rates[4], low temperature processability[5], and promise for ultra-low fabrication cost[6]. Over the past few years, the power conversion efficiency (PCE) of a single-junction perovskite photovoltaic device has been boosted from 3.8%[7] to a certified 22.1%[8], which is unprecedented. Despite the achievement of high PCEs, long-term stability suitable to deliver greater than 25 years outdoor operation remains un-proven.

Three-dimensional (3D) perovskite materials reported thus far, especially those based on the methylammonium (MA) cation, suffer from intrinsic instability and are prone to degradation upon exposure to moisture, heat, oxygen and UV-light irradiation[9–13]. The archetypal MA-based perovskite solar cells (*i.e.*, methylammonium lead triiodide: $MAPbI_3$) exhibit intrinsic thermal instability due to the relative volatility of MA cation, which released out of the film during heating, and this process is accelerated in the presence of moisture[13–15]. We have previously shown that formamidinium(FA)-based perovskites exhibit much greater thermal stability than MA-based perovskites[9,16]. However, $FAPbI_3$ is structurally unstable in the black perovskite phase, and undergoes a rapid phase transition to a yellow non-perovskite phase in ambient conditions at room temperature. To overcome this structural instability, an inorganic cation, caesium (Cs) can be incorporated into the $FAPbI_3$ which structurally stabilises the FA-based perovskite owing to its small ionic radius, and specifically enhances its structural stability, eliminating the black-to-yellow phase transition in humid air[16–18]. Recently, we have demonstrated that the FA/Cs-based solar cells are nearly 30 times more stable than the conventional MA-based cells under full sun illumination in ambient conditions[11], highlighting that FA/Cs perovskite is a promising candidate for stable perovskite solar cells.

In addition to developing resilient 3D perovskite materials, another approach to improving device stability is to employ two-dimensional (2D) Ruddlesden–Popper phase layered perovskites [*i.e.* $(RNH_3)_2(A)_{n-1}BX_{3n+1}$, where RNH_3 are large

alkylammonium cations acting as a spacer between the perovskite layers, and the A and B cations and X anions form the perovskite framework[19,20]] as the photoactive layers, which have shown superior moisture stability over 3D methylammonium based perovskites[21,22]. However, until recently, perovskite solar cells employing layered perovskite compounds have exhibited relatively low efficiency (PCE < 10%)[21,23], assumed to be due to the inhibition of out-of-plane charge transport by the insulating spacer cations. Tsai and co-workers recently adopted a "hot-casting" technique to fabricate highly crystalline $(BA)_2(MA)_3Pb_4I_{13}$ (BA: *n*-butylammonium, $C_4H_9NH_3$) Ruddleson-Popper phase perovskite films with the insulating spacer cations aligned along the out-of-plane orientation which facilitates efficient charge transport along the perovskite planes, achieving a 12.5% efficient layered perovskite solar cell with improved moisture and light stability[24]. Despite of the significantly enhanced stability, the application of 2D perovskites in photovoltaics are limited by their short carrier diffusion length, low carrier mobility and narrower absorption windows[19,21,22,25]. More recent efforts involving 2D perovskites has been focussed on tuning the '*n*' values, *i.e.* the perovskite dimensionility[25–28]. However, the enhanced air stability is still at the cost of the desirable optoelectronic properties.

Herein, we introduce *n*-butylammonium cations into a "mixed-cation lead mixed-halide" $FA_{0.83}Cs_{0.17}Pb(I_xBr_{1-x})_3$ 3D perovskite, in order to form a novel mixed-ion perovskite absorber. We investigate the impact of the BA cations on the intermediate phases in the precursor films, which allow us to modulate the initial nucleation and the subsequent crystallisation kinetics. We observe the formation of 2D perovskite platelets, interspersed between highly orientated 3D perovskite grains, which suppress charge recombination. We investigate the relationship between thin film composition, crystal alignment and device performance, and find an optimum BA composition which increases the power conversion efficiency of the solar cells to over 20%, and further enhances the long-term stability of the FA/Cs based mixed-cation lead mixed-halide perovskite solar cell.

Results and discussion

BA/FA/Cs perovskite precursor films. The perovskite films in this study are based on mixed-cation lead mixed-halide $FA_{0.83}Cs_{0.17}Pb(I_{0.6}Br_{0.4})_3$ composition unless otherwise stated. We note that the stated composition is based on the composition of the starting solution and the precise composition of the final film may vary. We tune the BA-to-FA/Cs mixing ratio by substituting different amount of FA/Cs (fixed at a molar ratio of 0.83:0.17 in the starting solution) cations with BA cations. We tested a series of

$BA_x(FA_{0.83}Cs_{0.17})_{1-x}Pb(I_{0.6}Br_{0.4})_3$ precursor compositions from x = 0 [*i.e.*, pristine $FA_{0.83}Cs_{0.17}Pb(I_{0.6}Br_{0.4})_3$] to x = 1, and the molar ratio of $BA_x(FA_{0.83}Cs_{0.17})_{1-x}$ to $Pb(I_{0.6}Br_{0.4})_3$ is kept at 1 : 1. We use *n*-butylammonium iodide powder as the BA^+ source in the precursor solutions and the total I/Br ratio in the solutions was kept constant at 0.6/0.4. We also acknowledge that we do not expect the x = 1, $BAPb(I_{0.6}Br_{0.4})_3$, to form a homogeneous 3D perovskite nor a homogeneous layered perovskite $BA_2Pb(I_{0.6}Br_{0.4})_4$, since the BA cation is too large to fit into the 3D perovskite structure and we have not added the appropriate stoichiometry to form the fully layered perovskite.

Generally, fabrication of perovskite films from a starting precursor solution to a final film undergo a complex crystallisation process, including nucleation and often a crystalline precursor phase formation, and subsequent perovskite crystal growth. Changes in a precursor solution (*i.e.*, using different types of cations) is likely to impact the crystal structure and morphology of the final films, which determine the ultimate solar cell device performance. In **Fig. S1** we show photographs, ultraviolent-visible (UV-Vis) absorption and photoluminescence (PL) spectra of "precursor" films after spin-coating and drying, but prior to crystallisation. We do indeed observe a strong impact of the addition of BA^+ which results in an increase in the absorbance and PL of the precursor films.

BA/FA/Cs crystallised perovskite films. To obtain the final perovskite films, we anneal the precursor films at 175 °C for 80 minutes in air. We first assess if there is any morphological change upon BA incorporation. In **Fig. 1**, we show scanning electron microscope (SEM) images of perovskite films with different BA concentrations. The pristine FA/Cs perovskite film (*i.e.*, x = 0) displays dense, pinhole-free morphology with 2 to 5 micron-size grains. By substituting 3% FA/Cs with BA (*i.e.*, x = 0.03), we observe an increase in the average grain size and simultaneously "plate-like" crystallites emerge. By further increasing the BA content to x = 0.09 and 0.16, we observe increasing amount of these plate-like crystallites, which appear to be interspersed between the larger "flat" grains. We tentatively suggest that these plate-like crystallites are composed of layered phases incorporating BA. With further addition of BA, the average grain size appears to shrink again.

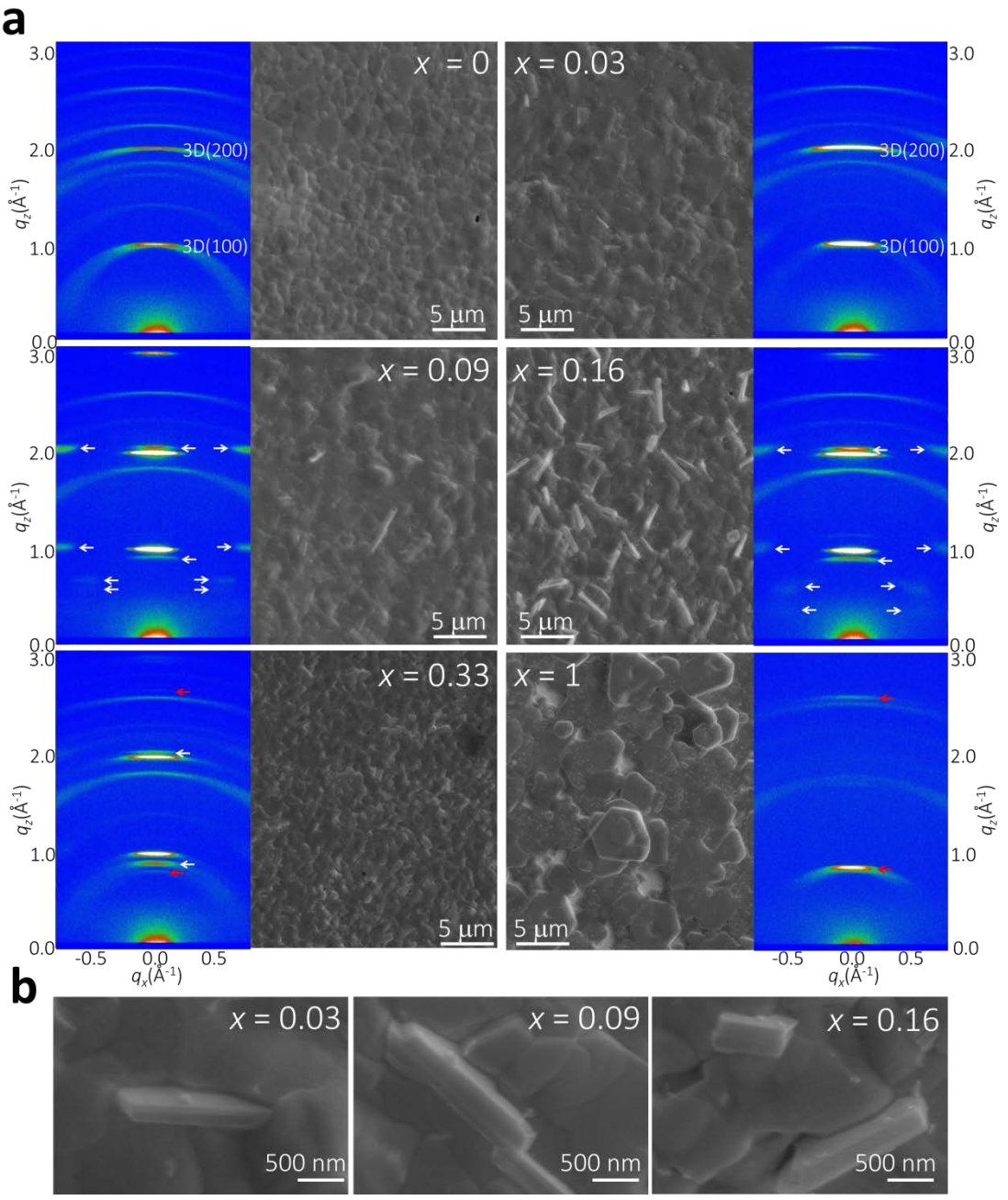

Figure 1. Morphology and crystal phases. a, SEM images of post-annealed perovskite films with different BA concentration, the insets show two-dimensional X-ray diffraction images. The arrows highlight diffraction patterns of the new phases. **b**, Enlarged SEM images.

In order to study the crystal structure of the perovskite films, we perform 2D X-ray diffraction (XRD^2) measurements[29], which allows us to measure a large portion of reciprocal space simultaneously[24]. In **Fig. 1a** (insets) we show XRD^2 images of

perovskite films with different BA concentrations. In the $x = 0$ film, we can assign all observed reflections to either the 3D $FA_{0.83}Cs_{0.17}Pb(I_{0.6}Br_{0.4})_3$ perovskite (in the primitive cubic setting; $a = b = c = 6.22$ Å, $\alpha = \beta = \gamma = 90^o$)[16] or the polycrystalline FTO substrate, which we show in **Fig. S3**. We determine from the XRD^2 data, in the $x = 0$ film the 3D perovskite phase displays some degree of texture compared to the archetypical $CH_3NH_3PbI_3$ perovskite[16,30]. With the introduction of BA, we observe a significant further increase in the peak intensities of the (*h*00) reflections in the XRD^2 scans and a disappearance of the powder diffraction rings, indicative of a much greater preference for the [100] direction to align parallel to the film normal. Furthermore, in the specular $2\theta/\omega$ scan, which we show in **Fig. S3**, the peak intensities of the (*h00*) reflections increase by a factor of 10, and in addition, all other (*hkl*) reflections disappear. In addition to the increased ordering of the 3D perovskite layer, we also observe additional reflections as we increase the BA concentration. Of particular note, is the observation of several off-specular reflections (which we mark with white arrows in **Fig. 1a insets**). These reflections cannot arise from the orientated 3D perovskite, since they are too low in 2θ and too close to the specular direction. They therefore arise from additional phases with larger *d*-spacing than the 3D perovskite. The phases responsible for these lower angle reflections are also notably orientated, since we do not observe powder diffraction rings. These new reflections are coincident with the appearance of the plate-like structures which we observed in the SEM images, and we thus assign the additional reflections to these structures. Since BA is known to form layered perovskite phases when mixed with MA in $(BA)_2(MA)_{n-1}PbI_{3n+1}$, we assume that the platelets we observe here are composed of $(BA)_2(FA_{0.83}Cs_{0.17})_{n-1}Pb(I_{0.6}Br_{0.4})_{3n+1}$ phases, likely orientated with their longest crystallographic axis in the sample plane, consistent with the emergence of lower 2θ angle reflections[24,31]. We cannot however assign the precise *n*-value, or composition of *n*-values, from our XRD^2 data, due to the low scattering volume of these platelets and the likelyhood of multiple-phases (*i.e.*, a mixture of different '*n*' values).

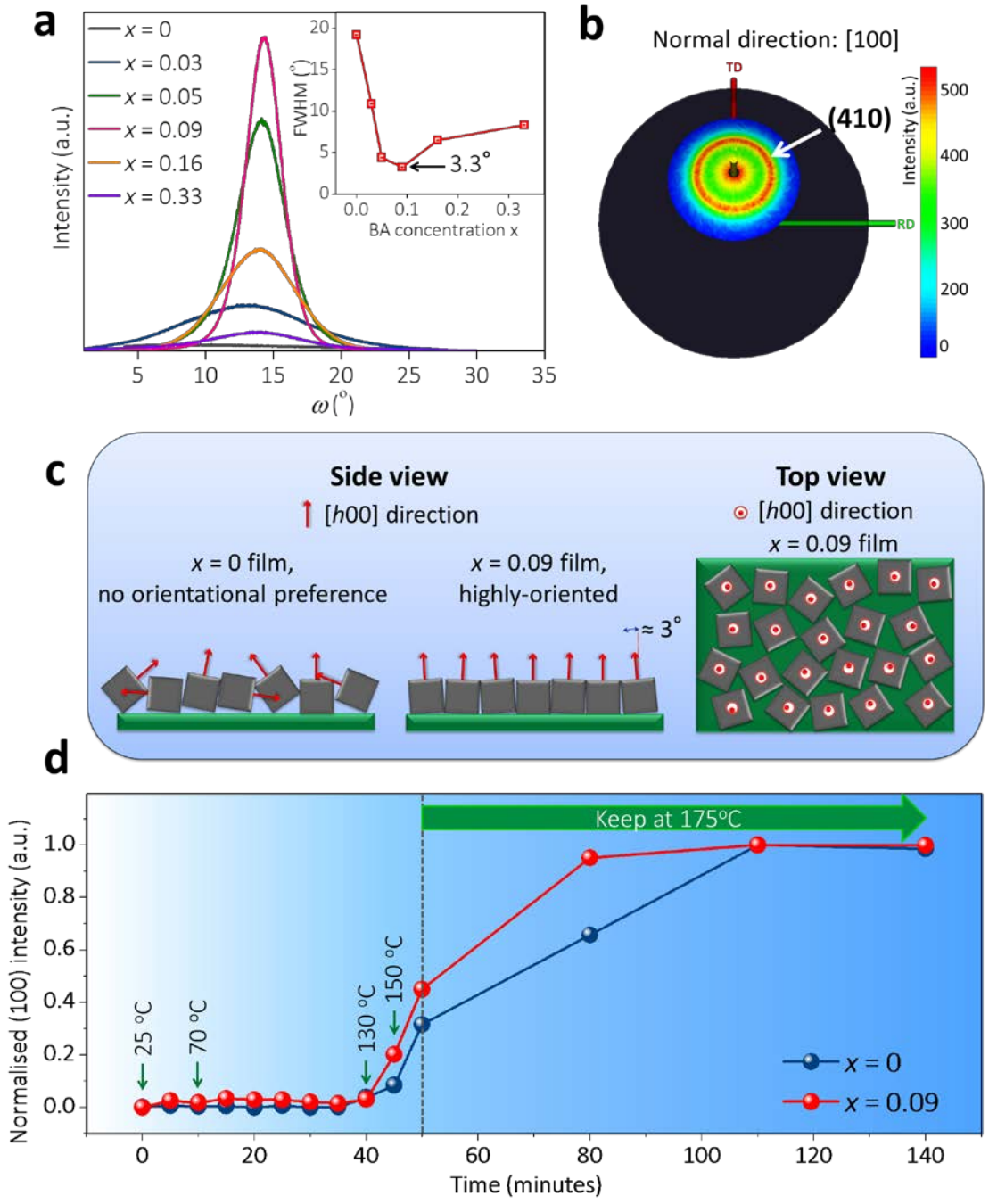

Figure 2. BA-enhanced 3D perovskite crystalline growth. a, X-ray diffraction rocking curves of the 3D perovskite (200) reflections with varying BA concentrations. The inset shows the FWHM values of the rocking curves. **b**, Pole figure of the (410) reflection of the 3D perovskite phase in the x = 0.09 film. RD and TD represent rolling direction and transverse direction, respectively, within the plane. The [100] direction defines the surface normal direction. **c**, Illustration, depicting the orientation of the 3D

perovskite phase in the x = 0.09 film, compared to a low-textured x = 0 film, showing a preference for [h00] direction to align out-of-plane and no orientation preference within the plane. Note that these squares just schematically illustrate the crystal orientation rather than the crystal grains. The real grains impinge together forming dense, pinhole-free morphology as we observed in the SEM images. **d**, Intensity of (100) reflection as a function of time during the perovskite annealing procedure (from room temperature to 175 ^{o}C) for two different BA concentrations (x = 0 and 0.09).

In order to further assess the distribution of orientations of the crystalline grains within the films, known as mosaicity[32,33], we measure rocking curves of the (200) reflections of the 3D perovskite phase, which we show in **Fig. 2a**. Whereas a $2\theta/\omega$ scan primarily characterises the crystallographic phases, their d-spacing and associated lattice strain, a rocking curve is the most reliable measure of the average orientation of a particular crystallographic phase. For example, the full-width half-maximum (FWHM) of a rocking curve (ω scan) is a direct measure of the deviation of the crystallographic grains from their average orientation; in a polycrystalline film with completely random grain orientation the FHWM would be undefined (ignoring instrumental and geometrical effects the rocking curve would be constant) and for a perfectly orientated single crystal it would be zero; values in between represent disorder in the average orientation of the crystallographic grains. For our control perovskite film (*i.e.*, x = 0), we cannot determine a precise rocking curve, which is consistent with a polycrystalline film with a low degree of texture. In contrast, all the films crystallised with the addition of BA clearly show resolvable rocking curves. In the low BA regime (x = 0.03) the FWHM of the (200) reflection is 11.2°. The (200) FWHM continues to reduce until at x = 0.09 we observe a minimum FHWM of 3.3°; this low value implies that the FA/Cs 3D perovskite phase greatly favours the orientation of the [100] direction parallel to the film normal (equivalently described as a preference for the (h00) planes to be parallel with the sample plane) when crystallising in the presence of BA. On increasing the BA concentration further to x = 0.16 and 0.33, we begin to see a broadening of the (200) rocking curve, but these compositions still display a preferred orientation.

The well-defined surface normal direction, [100], of the x = 0.09 film allows us to investigate the 3D perovskite crystal orientation within the sample plane by performing a pole figure measurement of the (410) reflection[34], shown in **Fig. 2b**. We observe a continuous ring of intensity as the sample is rotated about the [100] direction, indicating that there is no preferential orientation of the crystal grains within the sample plane. This result, along with the rocking curve of the x = 0.09 film, allows us to fully describe

the orientation of the 3D perovskite phase as fully disordered within the sample plane but a high preference for the [100] direction to be aligned parallel to the film normal, as we summarised in **Fig. 2c**. In order to investigate the mechanism driving the increased crystallinity and orientation of the perovskite grains with addition of BA, we further monitor the peak intensity of the (100) reflection as a function of time during annealing, for the x = 0 and x = 0.09 films, as we show the data in **Fig. 2d**. The crystallisation in the films in the presence of BA is accelerated, with the crystallisation evolving faster, to a much higher degree of crystallinity, the mechanism of which will be discussed in the later section.

Apart from the enhanced crystallinity of the 3D perovskite in the self-assembled BA/FA/Cs perovskite films, the modification of the thin-film growth might also induce changes in the lattice parameter of 3D perovskite. To obtain the lattice constant, we used least-squares refinement of a Lorentzian profile to fit the (100) Bragg reflection of the 3D perovskite, as we show in **Fig. S4a**. In **Fig. S4b**, we clearly observe that the lattice constant of the 3D perovskite decreases with increasing BA content; decreasing from a = 6.22 Å to 6.18 Å (~ 0.6%). Changes in lattice constant can be caused by incorporation of foreign ions (*i.e.*, BA cations in this work), changes in the strain, or changes in halide composition. In the case of FA/Cs substituted by the BA cation in the 3D perovskite crystal structure, we would expect an increase in the lattice constant due to the larger ionic radius of BA^+. Additionally, due to its larger size, we would not expect BA^+ to be able to be incorporated within the 3D perovskite structure[35,36]. Therefore, the reduced lattice constant could be either due to a change in the lattice strain, potentially due to the 3D perovskite grains interfacing with the layered phases, or simply released strain due to the significant reduction in the mosaicity of the film. Alternatively, the reduced lattice constant may be due to the precise I/Br composition in the crystalized perovskite film varying with the BA addition, possibly imposed by the change in crystallization kinetics. We note, however, that if we fix the total Br to I composition in the starting solution at 0.4 to 0.6, we do not know the precise final composition in the crystallised films. We also note that a lattice contraction of 0.6% is consistent with a change in Br/I composition from 0.4/0.6 to 0.43/0.57, and we would expect a corresponding band gap reduction of 30 meV[16].

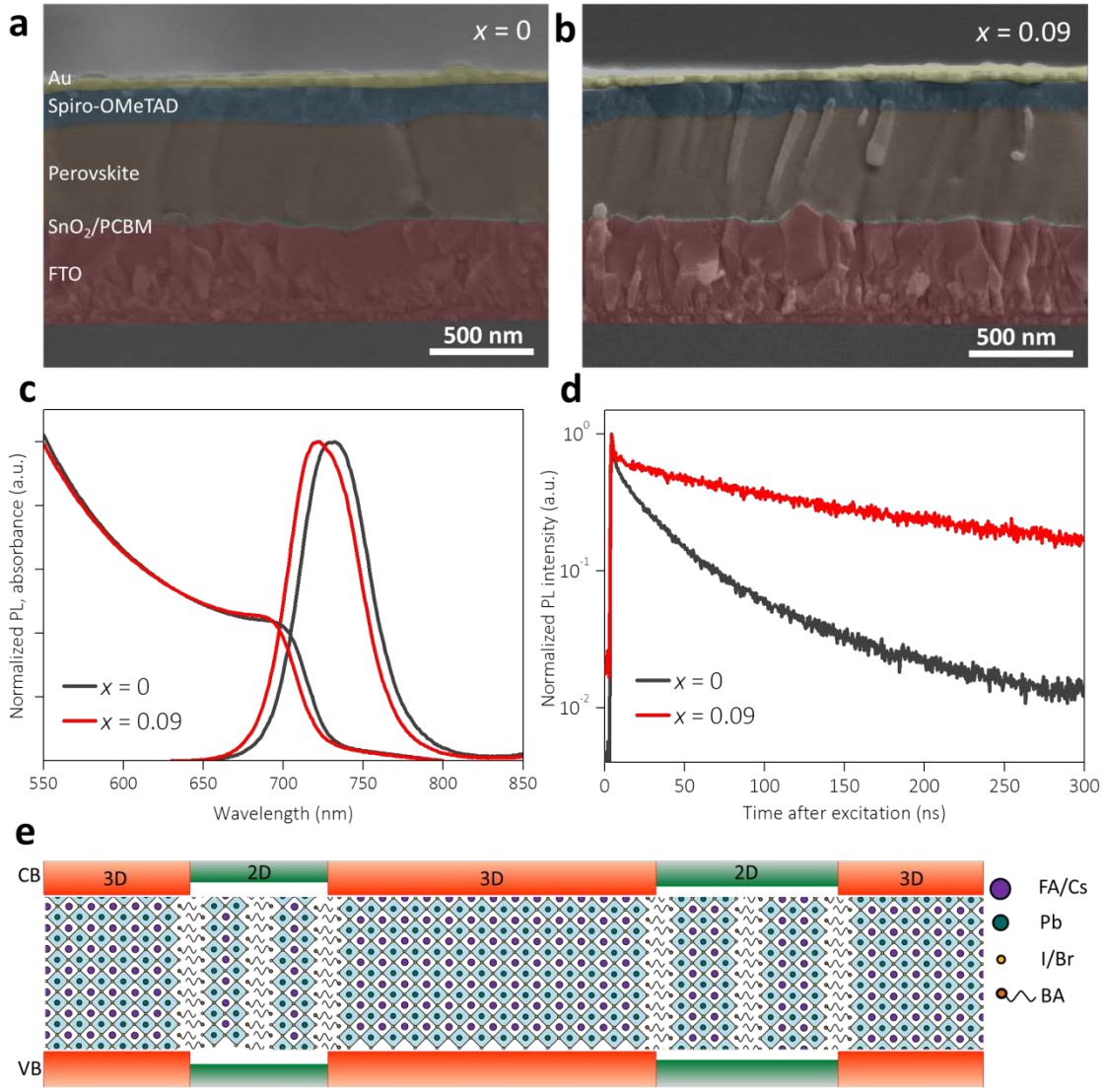

Figure 3. 2D-3D perovskite heterostructure. Cross-sectional SEM images of **a**, $FA_{0.83}Cs_{0.17}Pb(I_{0.6}Br_{0.4})_3$ (x = 0) film, and **b**, $BA_{0.09}(FA_{0.83}Cs_{0.17})_{0.91}Pb(I_{0.6}Br_{0.4})_3$ (x = 0.09) film. **c,** UV-Vis absorption and photoluminescence (PL) spectra. **d**, Time-resolved PL spectra. **e**, Schematic illustration of the proposed self-assembled 2D-3D perovskite film structure and corresponding electronic heterojunction band offsets.

In order to investigate if the plate-like features extend throughout the film, we show the cross-sectional SEM images of the x = 0 and x = 0.09 perovskite films incorporated into complete photovoltaic devices in **Fig. 3**. We clearly observe some thin crystals, vertically aligned in the x = 0.09 film. These crystals are of similar size and width to the thin platelets we observed in the surface-view SEM images (**Fig. 1**), consistent with these platelets being orientated in the perpendicular direction to the substrate. This

additional information allows us to form a clear understanding of the role of BA in the crystallisation of the FA/Cs perovskite film. The BA cations are expelled from the crystallising 3D perovskite domains as crystallisation proceeds, but appear to act as a flux, accelerating the crystal growth. Since the 3D domains are preferentially aligned with the (010) plane perpendicular to the plane of the substrate, the only means by which the 2D perovskite phase can interface well with the 3D perovskite phase, without a significant energetic cost, is for the 2D phases to also align with their (010) plane perpendicular to the plane of the substrate, with the longest crystallographic axis lying in the sample plane. Fortuitously, in this orientation the lattice constant in the plane of the lead halide sheet of the layered perovskite phase is very close to the lattice constant in the 3D perovskite phase. Therefore there is a good possibility that lattice matching will occur between these phases, which could be electronically advantageous. We note, that since the halides, FA and Cs cations are relative diffusive within the perovskite films, it will be feasible for the precise mixed A-site and halide compositions to be dissimilar within the 3D and 2D platelet phases, which should facilitate easier lattice matching. With the 100% BA, the grains appear to lie flat in the plane of the film, and at some critical concentration at around $x = 0.33$, the platelet features appear to preferentially lay down. This change in orientation of the platelets is likely to reduce the surface energy of the film, once the concentration of platelets exceeds a certain threshold.

In order to assess if this compositionally heterogeneous film is advantageous or disadvantageous concerning light absorption and charge recombination, in **Fig. 3c** and **3d**, we present UV-vis absorption and PL spectra, and time resolved PL traces for the post-annealed films. With the introduction of BA we observe a slight blue shift in the PL position, likely to originating from the, previously discussed, slight shrinkage of the 3D crystal lattice. We also observe that the addition of BA significantly increases the PL lifetime of the perovskite films, consistent with a significant reduction in the recombination in the films. This is indicative that the presence of the 2D platelets suppresses charge recombination.

With the above observations we postulate that the 2D perovskite phases interface with the 3D phases at locations where grain boundaries between 3D domains would have otherwise been present. Since this heterojunction between 2D and 3D phases inhibits charge recombination, we assume that the crystallographic connectivity between the two phases is good, without a significant density of crystal defects, and hence presents a clean electronic interface. Since the band gaps of the layered perovskite phases are wider than the band gap of the 3D phases[37], the electronic

configuration across the 2D-3D heterojunction will be similar to a classical type-I or type-II heterojunction[38]. We illustrate such a type-I configuration in **Fig. 3e**. Therefore, when charges reach this interface from within the 3D grain, they will be reflected remaining in the 3D perovskite and not suffer from trapping and recombination at the grain boundaries. If the conduction and valance band of the layered phase are offset, with respect to those of the 3D phase, as is the case for a type-II heterojunction, then one carrier (electron or hole) would be reflected from the heterojunction and the other would pass through.

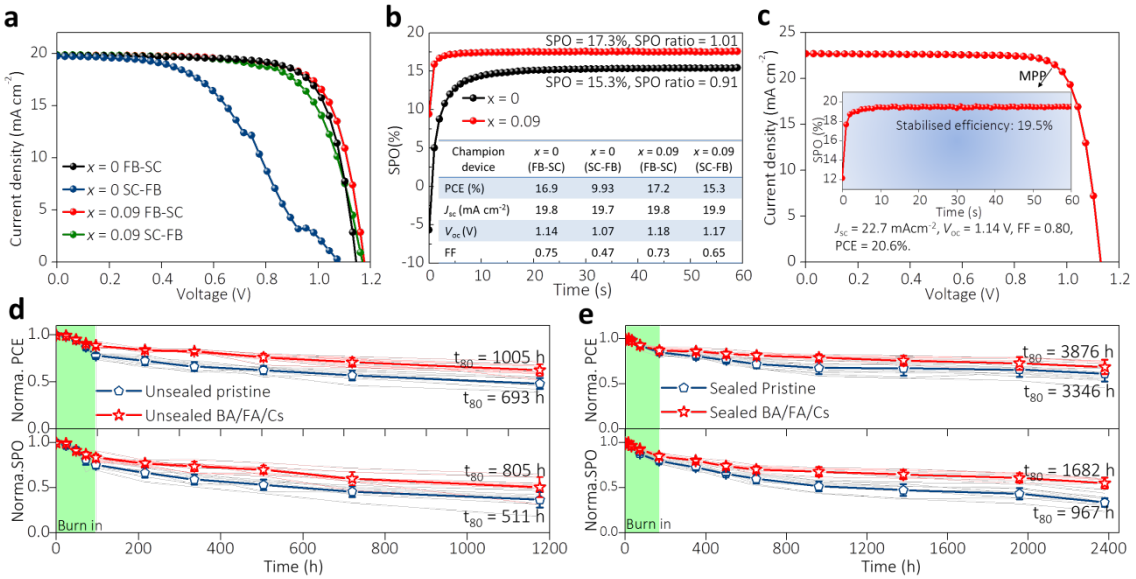

Figure 4. **Device performances of the BA/FA/Cs perovskite solar cells. a**, *J–V* characteristics of optimized perovskite solar cells using $FA_{0.83}Cs_{0.17}Pb(I_{0.6}Br_{0.4})_3$ (labelled as x = 0) and $BA_{0.09}(FA_{0.83}Cs_{0.17})_{0.91}Pb(I_{0.6}Br_{0.4})_3$ (labelled as x = 0.09) perovskite active layers, measured from forward bias (FB) to short-circuit (SC) and back again. **b,** Stabilised power output (SPO) of the champion cells, determined by holding the cell at a fixed voltage near the maximum power point (MPP) on the *J–V* curve for 60 s, the SPO ratio stands for the ratio between the SPO and *J–V* scanned efficiency. **c**, *J–V* characteristic of a best performing perovskite solar cell using $BA_{0.05}(FA_{0.83}Cs_{0.17})_{0.95}Pb(I_{0.8}Br_{0.2})_3$ active layer, the inset shows the corresponding SPO data. **d**, **e**, Comparison of stability of high-performance non-encapsulated (**d**) and encapsulated (**e**) solar cell devices using $FA_{0.83}Cs_{0.17}Pb(I_{0.6}Br_{0.4})_3$ (labelled as pristine) and $BA_{0.09}(FA_{0.83}Cs_{0.17})_{0.91}Pb(I_{0.6}Br_{0.4})_3$ (labelled as BA/FA/Cs) perovskite active layers. The devices are aged under xenon lamp simulated full spectrum AM1.5, 76 mW cm^{-2} equivalent irradiance in air without any UV filter, held at open-circuit during aging, and tested at different time intervals under a separate AM1.5 100mW cm^{-2} solar simulator. The Suntest XLS+ aging box irradiates pulsed light. There is an early burn-in with an

exponential decay over the first ~100 h followed by an approximate linear decay. The light grey and red lines in (**d**) and (**e**) display the actual efficiency decay of eight pristine devices and eight BA/FA/Cs devices, respectively. The navy blue and red lines show the averaged device efficiency decays. The time to 80% of the post burn-in decay (t_{80}) of champion devices is shown on the graph (with the t_0 efficiency extrapolated back to the y-axis from the linear fit, as shown in **Fig. S12 and S13**). The cell structure is glass/FTO/SnO_2/fullerene/perovskite/spiro-OMeTAD (with Li-TFSI and tBP additives)/Au. We note that PCBM is employed as the n-type fullerene for the devices in (**a**), (**b**) and (**c**), and C_{60} in the devices reported in (**d**) and (**e**).

Photovoltaic performance. To assess if the BA/FA/Cs perovskite can enhance the solar cell performance, we have fabricated and optimized devices based on a negative-intrinsic-positive (n–i–p) planar heterojunction architecture: glass/FTO/SnO_2/fullerene/perovskite/spiro-OMeTAD/Au. Through testing a series of BA concentrations, we find that the devices with $BA_{0.09}(FA_{0.83}Cs_{0.17})_{0.91}Pb(I_{0.6}Br_{0.4})_3$ perovskite (*i.e.*, x = 0.09) exhibit statistically improved performances, as we show in **Fig. S5**. In **Fig. 4a**, we show current density voltage (*J–V*) characteristics of champion devices measured under simulated AM1.5G solar irradiance at 100 mW cm^{-2} and give the full performance statistics of the entire device series and typical external quantum efficiency (EQE) spectrum in **Fig. S6** and **Fig. S7**, respectively. The champion BA/FA/Cs perovskite device, with a perovskite band gap of 1.72 eV, exhibits a short-circuit current (J_{sc}) of 19.8 mA cm^{-2}, a fill factor (FF) of 0.73, and an open-circuit voltage (V_{oc}) of 1.18 V, yielding a PCE of 17.2%. The control device (*i.e.*, x = 0) exhibits significant *J-V* hysteresis when scanning the photocurrent with reverse or forward bias at a scan rate of 380 mVs^{-1}. In contrast, the BA/FA/Cs device exhibits a significant reduction in *J-V* hysteresis. Anomalous hysteresis is mainly caused by the migration of ionic species to the grain boundaries and perovskite thin film interfaces, which then modulate the trap assisted, or surface, recombination[39,40]. To gain a better understanding of the reduced hysteresis, we determine the stabilised power output (SPO)[41] by measuring the current at a fixed maximum power point (MPP) voltage over 60 s, which we show in **Fig. 4b**. Under constant operation, the efficiency of the control device rises over 15 s to reach a stabilised value of 15.2% with an SPO-to-PCE ratio (so-called 'SPO ratio') of 0.91. In contrast, the "x = 0.09" device stabilises within 5s at a higher value of 17.3%, yielding an SPO ratio of 1.01. The faster stabilising rate and the higher SPO ratio is consistent with the perovskite film having a lower density of trap-sites responsible for trap-assisted recombination[42], consistent with our measured

enhancement in the PL lifetime. For polycrystalline perovskite solar cells, minimizing the charge recombination at grain boundaries is likely to be of great importance in reducing device hysteresis[43]. It appears that the presence of the 2D-3D heterostructure within these films has successfully alleviated hysteresis.

By further employing a narrower bandgap $BA_{0.05}(FA_{0.83}Cs_{0.17})_{0.95}Pb(I_{0.8}Br_{0.2})_3$ perovskite as a photoactive layer, we are able to achieve a champion *J-V* measured PCE of 20.6% and a stabilised power output of 19.5%, as we show in **Fig. 4c** (also see the device characteristics and the EQE spectrum in **Table S1, Fig. S8 and S9**). We note that the bandgap of the perovskite are derived using a Tauc plot from the UV-vis absorption spectrum[44] which matched with the effective band gap assessed by the inflection point of the EQE spectrum[45], as we show in **Fig. S10**.

We have previously found that the FA/Cs based perovskites require spin-coating in a nitrogen filled glove box in order to achieve smooth and uniform films. Here, we find that the perovskite films incorporating BA have excellent processability in air under a relatively high humidity level (~ 45 RH%). As we show in **Fig. S11**, the pristine film processed in humid air shows a discontinuous morphology containing a large amount of pinholes, while the BA/FA/Cs based perovskite film show a pinhole-free morphology and greatly enhanced crystallinity. The BA-based device processed in air shows a champion efficiency of 14.3% which is 2.5 times larger than the pristine FA/Cs device efficiency of 5.9%. This technique has great potential in a scalable commercial process for fabricating perovskite devices without the requirement for a stringently controlled manufacturing environment.

Device stability. Our primary motivation for the inclusion of BA within the FA/Cs mixed cation perovskite was to examine if this can further enhance the long term stability of such a material. To examine whether the BA/FA/Cs perovskite has an impact upon device stability we perform aging tests of high performance non-encapsulated and encapsulated perovskite devices based on the wide bandgap (1.72 eV) $FA_{0.83}Cs_{0.17}Pb(I_{0.6}Br_{0.4})_3$ perovskite under full spectrum simulated AM1.5 sun light, at 76 mA cm^{-2} irradiance without a UV filter in air with ambient humidity (~ 45 RH%). We note that we employ SnO_2/C_{60} as an electron-transporting layer (ETL) for the stability test, although there is a slight improvement in the “as fabricated” efficiency when employing SnO_2/PCBM as the ETL. As we show in **Fig. 4d**, we observe that the BA/FA/Cs non-encapsulated devices exhibit enhanced long-term stability, in comparison to the control FA/Cs device in both of the *J–V* scanned PCE and the SPO.

This improvement primarily arises from the retarded photocurrent decay, as we show in **Fig. S12**, where we present all the *J-V* performance parameters. To perform a quantitative analysis, we fit the post "burn in" section of the PCE to a straight line and extrapolate the curve back to zero time to obtain the $t = 0$ efficiency[11]. We determine the lifetime to 80% degradation (t_{80}) from this $t = 0$ post burn-in efficiency[46] for the most stable BA/FA/Cs devices to be 1,005 hrs, and the SPO t_{80} lifetime is 805 hrs. This is nearly 50% longer than the t_{80} lifetime of the control FA/Cs device[11], and the surpassing of 1,000 hrs stability for an unsealed perovskite cell under these conditions marks a clear milestone in the progress towards perovskite solar cells and modules with industrially acceptable stability. We further proceed to encapsulate the devices with a hot melt polymer foil and a glass coverslip and show the stability results in **Fig. 4e** and **Fig. S13**. For the BA/FA/Cs perovskite devices, we achieve a champion t_{80} lifetime of 3,876 hrs for the *J-V* measured PCE and 1,682 hrs for the SPO. We note that the control FA/Cs devices exhibit a champion t_{80} lifetime of 3,346 hrs, which is very close to the value for the BA/FA/Cs device. In contrast, the champion SPO t_{80} lifetime of the encapsulated FA/Cs device is only 967 hrs, which is 40% lower than the BA/FA/Cs device. We note that the observation of a faster decay in the SPO versus measured PCE is consistent with an increase in the density of defects responsible for trap-assisted recombination occurring during aging. Following from our understanding of *J-V* hysteresis, the scanned efficiency is insensitive to small changes in the density of defects responsible for trap assisted recombination, because electronic biasing during the measurements result in ion migration which favourably stabilises trapped charge at the charge collection interfaces. On the other hand, under steady state operation near MPP the ions redistribute and the degree of favourable trap passivation is reduced, making the SPO more sensitive to increases in trap densities. Hence, since the SPO of the control device drops faster than the SPO of the BA/FA/Cs device, we can infer that the defects form faster in the devices absent of BA. Our results demonstrate a near doubling of the long-term stability in a like-to-like comparison with the control, FA/Cs cells, which were previously the most stable perovskite composition[11,16,47]

We believe that there are a number of advancements in BA/FA/Cs perovskite which contribute to the enhanced stability.

Firstly, we have observed that introduction of the BA cations greatly improves the

crystal orientation of 3D perovskite grains and overall crystallinity in the material, indicative of a reduced number of bulk crystal defects. The degradation of the perovskite films is likely to proceed via active defects[48] and hence reducing the number of defects is very likely to positively improve the long term stability.

Secondly, the presence of the layered perovskite phases at the grain boundaries is likely to inhibit degradation proceeding via the grain boundaries. Recently, Wang *et al*. reported that the moisture-induced degradation of 3D perovskite films start from grain boundaries[49]. Therefore, "coating" 3D perovskite grains with either stable layered perovskite crystallites, or simply a shell of butylammonium, will help to protect the perovskite film from moisture, directly contributing to the stability enhancement.

Conclusion

In conclusion, we have demonstrated a novel mixed-cation lead mixed-halide BA/FA/Cs perovskite system, exhibiting significantly improved device efficiency and operational stability. By carefully regulating the BA content, we appear to obtain plate-like "layered" perovskite crystallites orientated perpendicularly to the plane of the film, embedded between 3D perovskite grains. With this unique heterostructure, photo-generated charges can transport freely in the 3D domains without hindrance by the insulating BA cation and are "reflected" from the interface with the layered material, inhibiting trapping and recombination. The presence of the BA and or layered perovskite plates appear to reduce defects within the perovskite films, which reduces the device hysteresis. With this BA/FA/Cs hybrid perovskite, we achieved a PCE of 17.2% (stabilised at 17.3%) when employing a wide bandgap (1.72 eV) $BA_{0.09}(FA_{0.83}Cs_{0.17})_{0.91}Pb(I_{0.6}Br_{0.4})_3$ perovskite as a photoactive layer and 20.6% (stabilised at 19.5%) when using a narrow bandgap (1.61 eV) $BA_{0.05}(FA_{0.83}Cs_{0.17})_{0.95}Pb(I_{0.8}Br_{0.2})_3$ perovskite. We also find that the BA/FA/Cs perovskite devices exhibit significantly improved operational stability over the neat 3D perovskite devices. The non-encapsulated devices comprising the BA/FA/Cs perovskite absorber layer sustain 80% of their "post burn-in" efficiency after more than 1,000 hours stressing under full sun illumination in ambient conditions, which is 50% higher than the 3D device, and over 3,800 hrs when sealed in a glass/polymer-foil/glass laminate. Our work represents a significant step towards highly efficient perovskite solar cells having long-term operational stability commensurate with real world outdoor applications. Equally importantly, we have demonstrated that it is possible to create stable heterostructures within a perovskite film, comprised of 3D and 2D domains. The interface between these heterostructures appears to be electronically clean, and

resultantly inhibits unwanted trap-assisted recombination. We note that type I and type II heterostructures have been central to controlling surface recombination in III-V semiconductor devices, such as GaAs photovoltaics and GaN LEDs. Our findings open the possibility of developing much more controlled 2D-3D perovskite heterostructures, and investigating the optoelectronic processes occurring at these interfaces. We believe that this will prove to be an important direction for ongoing developments in perovskite solar cells and optoelectronic devices, and may deliver model systems for fundamental investigations.

Methods

Preparation of perovskite precursor: (1) *Formamidinium iodide synthesis:* $HC(NH_2)_2I$ (Formamidinium iodide, FAI) was synthesized by dissolving formamidine acetate (Sigma-Aldrich) powder in a 1.5 M excess of hydroiodic acid (HI; Sigma-Aldrich), 57 wt% in H_2O. After addition of the acid, the solution was left stirring for 10 minutes at 50 °C. Upon drying at 100 °C for approximately 2 hrs, a yellow-white powder is formed. This powder was then washed three times with diethyl ether to remove excess I_2. The powder was later dissolved in ethanol and heated at 80°C to obtain a supersaturate solution. Once fully dissolved, the solution is then placed in a refrigerator overnight for recrystallisation. The recrystallisation process formed white flake-like crystals. The FAI flakes were later washed with diethyl ether three times. Finally, the FAI flakes was dried overnight in a vacuum oven at 50°C. (2) *Preparation of BA/FA/Cs perovskite precursor solution*: we first fabricate $FA_{0.83}Cs_{0.17}Pb(I_{0.6}Br_{0.4})_3$ precursor solution by dissolving FAI, cesium iodide (CsI; Alfa Aesar), lead iodide (PbI_2; TCI) and lead bromide ($PbBr_2$; TCI) in anhydrous *N*,*N*-dimethylformamide (DMF; Sigma-Aldrich) to obtain a stoichiometric solution. The solution was then stirred overnight in a nitrogen-filled glovebox. We then add 69 µl of hydroiodic acid (HI; Sigma-Aldrich), 57 wt% in H_2O and 34.6 µl of hydrobromic acid (HBr; Sigma-Aldrich), 48 wt% in H_2O into 1 ml of 1.2 M $FA_{0.83}Cs_{0.17}Pb(I_{0.6}Br_{0.4})_3$ precursor solution, and age for approximately 48 hours under a nitrogen atmosphere without stirring. In parallel, we generate $BAPb(I_{0.6}Br_{0.4})_3$ precursor solution by dissolving *n*-butylammonium iodide (BAI; Dyesol), PbI_2 and $PbBr_2$ in DMF to obtain a stoichiometric solution. The solution was also stirred overnight in a nitrogen-filled glovebox. Prior to film deposition, we blend the $FA_{0.83}Cs_{0.17}Pb(I_{0.6}Br_{0.4})_3$ and $BAPb(I_{0.6}Br_{0.4})_3$ precursor solutions to achieve $BA_x(FA_{0.83}Cs_{0.17})_{1-x}Pb(I_{0.6}Br_{0.4})_3$ with desired BA contents. For $FA_{0.83}Cs_{0.17}Pb(I_{0.8}Br_{0.2})_3$ perovskite solution, we add 87.2 µl HI acid and 16.5 µl HBr acid to 1 ml of 1.2 M of the precursor solution and was aged for approximately 48 hours under a nitrogen

atmosphere without stirring. We then blend it with the $BAPb(I_{0.8}Br_{0.2})_3$ to achieve the $BA_x(FA_{0.83}Cs_{0.17})_{1-x}Pb(I_{0.8}Br_{0.2})_3$ precursor solution.

Substrates preparation: All the devices are deposited on fluorine doped tin oxide (FTO) coated glass substrates (Pilkington TEC 7). Initially, FTO was removed at specific regions where for the anode contact deposition. This FTO etching was done using a 2M HCl and zinc powder. Substrates were then cleaned sequentially in hallmanex detergent, acetone, ethanol, isopropyl alcohol, and dried with a compressed nitrogen gun. Thereafter, it was treated for 10 min in oxygen plasma.

Electron-transporting layer fabrication: Two electron-accepting layers have been discussed in this paper: (1) *SnO_2/doped $PCB_{61}M$*: Tin (IV) chloride pentahydrate ($SnCl_4 \cdot 5H_2O$) (Sigma-Aldrich) was dissolved in anhydrous 2-propanol (0.05 M) and stirred for 30 min. The solution was spin-coated at 3000 rpm for 30 s. The substrates were then dried at 100 °C for 10 min and annealed at 180 °C for 60 min. For doped PCBM layer, we dissolve PCBM (Solenne) in anhydrous 1,2-dichlorobenzene (DCB; Sigma-Aldrich) at 10 mg ml^{-1}. We dissolve the dopant 4-(1,3-dimethyl-2,3-dihydro-1Hbenzimidazol-2-yl)-*N*,*N*-diphenylaniline (*N*-DPBI; Sigma-Aldrich) dissolved in DCB at 10 mg ml^{-1}. Both of the PCBM and *N*-DPBI solutions were stirred overnight at room temperature. Prior to deposition, we add 20 µl of *N*-DPBI solution in 1 ml PCBM precursor solution. Then, we spin coat the doped PCBM solution on top of the as-prepared SnO_2 layer in a nitrogen-filled glovebox at 2500 rpm for 40 s, and annealed in nitrogen at 80 ^oC for overnight to achieve successful doping. (2) *SnO_2 nanoparticle/doped C_{60}*: The SnO_2 nanoparticles were synthesized via hydrothermal method, similarly to the method described by Zhang et al[50]. We dissolve 467 mg of $SnCl_4 \cdot 5H_2O$ (Sigma-Aldrich) in 20 ml of deionized water. After 10 minutes of stirring at room temperature, a fully dissolved, clear solution is obtained. This solution is then transferred to a Teflon-lined stainless steel autoclave and heated for 2 hours at 250^oC. After heat treatment, the autoclave is quenched to room temperature using cold water. The precipitates were centrifuged at a speed of 9000 rpm for 15 min. The nanoparticles were re-dispersed in ethanol. This washing treatment was repeated 3 times. After the final washing treatment, the nanoparticles were also re-dispersed in

ethanol. On the cleaned FTO substrates, a 2 mg ml^{-1} SnO_2 nanoparticle solution is spin coated in air at 2000 rpm for 45s, and annealed at 150 ^oC for 2 minutes. Similar to the PCBM doping procedure, we dope the 10 mg ml^{-1} C_{60} (Solenne) precursor solution with *N*-DPBI dopant to achieve 1 wt% *N*-DPBI/C_{60} doping ratio. The doped solution was then spin coated on the as-prepared SnO_2 nanoparticle layer at 1500 rpm for 60 s, and annealed in nitrogen at 80 ^oC overnight. More details are reported elsewhere[11].

Perovskite photoactive layer fabrication: The precursor perovskite solution was spin-coated in a nitrogen-filled glovebox at 2000rpm for 45s, on a substrate pre-heated at 80°C. The films were dried inside the glovebox on a hot plate at a temperature of 70°C for 60 seconds. The films were then immediately transferred in an oven and annealed in air at 175°C for 80 minutes.

Hole-transporting layer fabrication: After the perovskite films cool down to R.T., the 2,2',7,7'-Tetrakis[*N*,*N*-di(4-methoxyphenyl)amino]-9,9'-spirobifluorene (spiro-OMeTAD) solution was spin-coated on the perovskite layer at 2500 rpm for 40 s in a drybox (< 15 RH%) as a hole-transporting layer. To obtain a spiro-OMeTAD solution, we dissolve 85.7 mg spiro-OMeTAD (Borun Technology) in 1 ml anhydrous cholobenzene with additives of 28.8 µl tert-butylpyridine (*t*BP) and 20 µl lithium bis(trifluoromethylsulfonyl)imide (Li-TFSI) salt in acetonitrile (520 mg ml^{-1}). We note that the spiro-OMeTAD layer used in the cells for stability tests was doped with 27.5 µl tert-butylpyridine (*t*BP) and 8.9 µl lithium bis(trifluoromethylsulfonyl)imide (Li-TFSI) salt in acetonitrile (170 mg ml^{-1}). The whole spiro-OMeTAD doping process was carried out in a nitrogen-filled glovebox.

Electrode evaporation: An 80 nm gold electrode was thermally evaporated under vacuum of $< 9 \times 10^{-6}$ Torr.

Current−Voltage Measurements: The *J–V* curves were measured (2400 Series SourceMeter, Keithley Instruments) under simulated AM 1.5 sunlight at 100 mW cm^{-2} irradiance generated by an Abet Class AAB sun 2000 simulator, with the intensity calibrated with an NREL calibrated KG 5 filtered Si reference cell. The mismatch factor was calculated to be less than 1%. The active area of the solar cell is 0.0919 cm^{-2}. The

forward *J–V* scans were measured from forward bias to short circuit and the backward scans were from short circuit to forward bias, both at a scan rate of 380 mV s^{-1}. A stabilisation time of 10 s at forward bias of 1.4 V under illumination was done prior to scanning.

External quantum efficiency (EQE) measurement: EQE spectra were evaluated via custom-build Fourier transform photocurrent spectroscopy based on the Bruker Vertex 80v Fourier transform spectrometer. A Newport AAA sun simulator was used as light source and the light intensity was calibrated with a Newport-calibrated reference silicon photodiode.

UV-Vis absorption: UV-vis absorption spectra were measured using a Bruker Vertex 80v Fourier transform infrared spectrometer fitted with a reflection/transmission accessory.

Photoluminescence Spectroscopy: PL spectra were collected with an intensified charge coupled device (iCCD, PI-MAX4, Princeton Instruments), with each sample photoexcited by a 398 nm picosecond pulsed diode laser (PicoHarp, LDH-D-C-405M).

Scanning Electron Microscopy: The morphology of perovskite films was investigated using a SEM (Hitachi S-4300) at an accelerating voltage of 3–5 kV.

X-ray diffraction (XRD): The one-dimensional and two-dimensional X-ray diffraction spectra of the prepared films were measured using a Rigaku SmartLab X-ray diffractometer with $CuK_{\alpha 1}$ (1.54060 Å) and a HyPix-3000 2D hybrid pixel array detector.

Pole figure: A pole figure consists of performing a scan about the surface normal (a φ scan) with fixed 2θ, fixed ω, at a range of ω. The surface normal is required to be a well-defined crystallographic direction (in our case [100]) and the 2θ value is set for an off-specular reflection of choice, (410). ω is set to $\omega_{410} = \theta + \Delta\theta$, where $\Delta\theta$ is equal to the angle between the [410] and specular (surface-normal, [100]) direction. One then rotates the sample about the surface - normal while measuring the diffracted intensity in steps of ω about ω_{410}. In this way we can be absolutely sensitive to the in-plane

orientation of the crystal structure. If a 'ring' of constant intensity is observed there is no preferential orientation within the sample plane. Conversely, if *m* spots (where *m* is the multiplicity of the measured reflection) are observed the sample is fully ordered both along the surface normal and in the sample plane (*i.e.*, epitaxial films grown on single crystal substrates). A pole figure is of no value in a polycrystalline film as the sample scatters uniformly for all ω.

Stability test: For stability measurement, the perovskite devices were encapsulated with a hot melting polymer foil (Oxford PV) and a glass coverslip as a barrier layer in a nitrogen filled glove box. Before encapsulation, we blow the devices with nitrogen gun to remove any contaminations and stored in a nitrogen-filled glovebox for two days to remove any moisture residuals. All the devices were aged under full spectrum simulated AM1.5, 76 mA cm^{-2} irradiance at open-circuit condition using an Atlas SUNTEST XLS+ (1700W air-cooled Xenon lamp). We note that the light source is pulsed at 100Hz frequency. The chamber is air-cooled to have a temperature between 50–60 ^{o}C as indicated by a Black Standard Temperature (BST) control unit mounted inside the ageing box. We do not have particular control on the humidity and do not use any UV-filter during the aging process.

References

1. Ogomi, Y. *et al.* $CH_3NH_3Sn_x Pb_{(1-x)}I_3$ Perovskite Solar Cells Covering up to 1060 nm. *J. Phys. Chem. Lett.* **5,** 1004–1011 (2014).
2. Noh, J. H., Im, S. H., Heo, J. H., Mandal, T. N. & Seok, S. Il. Chemical management for colorful, efficient, and stable inorganic-organic hybrid nanostructured solar cells. *Nano Lett.* **13,** 1764–1769 (2013).
3. Stranks, S. D. *et al.* Electron-hole diffusion lengths exceeding 1 micrometer in an organometal trihalide perovskite absorber. *Science* **342,** 341–344 (2013).
4. Oga, H., Saeki, A., Ogomi, Y., Hayase, S. & Seki, S. Improved understanding of the electronic and energetic landscapes of perovskite solar cells: High local charge carrier mobility, reduced recombination, and extremely shallow traps. *J. Am. Chem. Soc.* **136,** 13818–13825 (2014).
5. Jeon, N. J. *et al.* Solvent engineering for high-performance inorganic-organic hybrid perovskite solar cells. *Nat. Mater.* **13,** 1–7 (2014).
6. Snaith, H. J. Perovskites: The Emergence of a New Era for Low-Cost, High-Efficiency Solar Cells. *J. Phys. Chem. Lett.* **4,** 3623–3630 (2013).
7. Kojima, A., Teshima, K., Shirai, Y. & Miyasaka, T. Organometal halide

perovskites as visible-light sensitizers for photovoltaic cells. *J. Am. Chem. Soc.* **131,** 6050–6051 (2009).

8. http://www.nrel.gov/ncpv/images/efficiency_charg.jpg. NREL efficiency chart. Available at: chart.jpg,. (Accessed: 17th April 2016)
9. Eperon, G. E. *et al.* Supplementary information Formamidinium of Formamidinium lead trihalide: a broadly tunable perovskite for efficient planar heterojunction solar cells. *Energy Environ. Sci.* **7,** 982 (2014).
10. Pearson, A. J. *et al.* Oxygen Degradation in Mesoporous Al 2 O 3 /CH 3 NH 3 PbI 3- x Cl x Perovskite Solar Cells: Kinetics and Mechanisms. *Adv. Energy Mater.* **6,** 1600014 (2016).
11. Wang, Z. *et al.* Efficient and Air-Stable Mixed-Cation Lead Mixed-Halide Perovskite Solar Cells with n-Doped Organic Electron Extraction Layers. *Adv. Mater.* **29,** 1604186 (2016).
12. Aristidou, N. *et al.* The Role of Oxygen in the Degradation of Methylammonium Lead Trihalide Perovskite Photoactive Layers. *Angew. Chemie - Int. Ed.* **54,** 8208–8212 (2015).
13. Leguy, A. M. A. *et al.* Reversible Hydration of CH3NH3PbI3 in Films, Single Crystals, and Solar Cells. *Chem. Mater.* **27,** 3397–3407 (2015).
14. Conings, B. *et al.* Intrinsic Thermal Instability of Methylammonium Lead Trihalide Perovskite. *Adv. Energy Mater.* **5,** (2015).
15. Misra, R. K. *et al.* Temperature- and component-dependent degradation of perovskite photovoltaic materials under concentrated sunlight. *J. Phys. Chem. Lett.* **6,** 326–330 (2015).
16. McMeekin, D. P. *et al.* A mixed-cation lead mixed-halide perovskite absorber for tandem solar cells. *Science* **351,** 151–155 (2016).
17. Yi, C. *et al.* Entropic stabilization of mixed A-cation ABX 3 metal halide perovskites for high performance perovskite solar cells. *Energy Environ. Sci.* **9,** 656–662 (2016).
18. Lee, J. W. *et al.* Formamidinium and cesium hybridization for photo- and moisture-stable perovskite solar cell. *Adv. Energy Mater.* **5,** 1501310 (2015).
19. Muljarov, E. A., Tikhodeev, S. G., Gippius, N. A. & Ishihara, T. Excitons in self-organized semiconductor/insulator superlattices: PbI-based perovskite compounds. *Phys. Rev. B* **51,** 14370–14378 (1995).
20. Stoumpos, C. C. *et al.* Ruddlesden-Popper Hybrid Lead Iodide Perovskite 2D Homologous Semiconductors. *Chem. Mater.* **28,** 2852–2867 (2016).
21. Smith, I. C., Hoke, E. T., Solis-Ibarra, D., McGehee, M. D. & Karunadasa, H. I.

A Layered Hybrid Perovskite Solar-Cell Absorber with Enhanced Moisture Stability. *Angew. Chemie - Int. Ed.* **53,** 11232–11235 (2014).

22. Cao, D. H., Stoumpos, C. C., Farha, O. K., Hupp, J. T. & Kanatzidis, M. G. 2D Homologous Perovskites as Light-Absorbing Materials for Solar Cell Applications. *J. Am. Chem. Soc.* **137,** 7843–7850 (2015).
23. Yao, K., Wang, X., Xu, Y. X., Li, F. & Zhou, L. Multilayered Perovskite Materials Based on Polymeric-Ammonium Cations for Stable Large-Area Solar Cell. *Chem. Mater.* **28,** 3131–3138 (2016).
24. Tsai, H. *et al.* High-efficiency two-dimensional Ruddlesden–Popper perovskite solar cells. *Nature* **536,** 312–316 (2016).
25. Quan, L. N. *et al.* Ligand-Stabilized Reduced-Dimensionality Perovskites. *J. Am. Chem. Soc.* **138,** 2649–2655 (2016).
26. Liao, Y. *et al.* with enhanced stability and photovoltaic performance Highly-oriented low-dimensional tin halide perovskites with en- hanced stability and photovoltaic performance. (2017). doi:10.1021/jacs.7b01815
27. Quan, L. N. *et al.* Tailoring the energy landscape in quasi-2D halide perovskites enables efficient green light emission. *Nano Lett.* acs.nanolett.7b00976 (2017). doi:10.1021/acs.nanolett.7b00976
28. Li, N. *et al.* Mixed Cation FAxPEA1?xPbI3 with Enhanced Phase and Ambient Stability toward High-Performance Perovskite Solar Cells. *Adv. Energy Mater.* **7,** (2017).
29. He, B. B., Preckwinkel, U. & Smith, K. L. Comparison between conventional and two-dimensional XRD. *Adv. X-ray Anal.* **46,** 37–42 (2003).
30. Tan, K. W. *et al.* Evolution and Performance of Solar Cells. 4730–4739 (2015). doi:10.1021/nn500526t C2014
31. Yuan, M. *et al.* Perovskite energy funnels for efficient light-emitting diodes. *Nat. Nanotechnol.* **11,** 1–27 (2016).
32. Ong, H. C., Zhu, A. X. E. & Du, G. T. Dependence of the excitonic transition energies and mosaicity on residual strain in ZnO thin films. *Appl. Phys. Lett.* **80,** 941–943 (2002).
33. Ko, H. J. *et al.* Improvement of the quality of ZnO substrates by annealing. *J. Cryst. Growth* **269,** 493–498 (2004).
34. Nagao, K. & Kagami, E. X-ray thin film measurement techniques: VII. Pole figure measurement. *Rigaku J.* **27,** 6–14 (2011).
35. Kieslich, G. *et al.* Solid-State Principles Applied to Organic-Inorganic Perovskites: New Tricks for an Old Dog. *Chem. Sci.* **5,** 4712–4715 (2014).

36. Filip, M. R., Eperon, G. E., Snaith, H. J. & Giustino, F. Steric Engineering of Metal-halide Perovskites with Tunable Optical Band Gaps. *Nat. Commun.* **5,** 5757 (2014).
37. Safdari, M. *et al.* Layered 2D alkyldiammonium lead iodide perovskites: synthesis, characterization, and use in solar cells. *J. Mater. Chem. A* **4,** 15638–15646 (2016).
38. Morozov, S. V. *et al.* Type II-type i conversion of GaAs/GaAsSb heterostructure energy spectrum under optical pumping. *J. Appl. Phys.* **113,** (2013).
39. Van Reenen, S., Kemerink, M. & Snaith, H. J. Modeling Anomalous Hysteresis in Perovskite Solar Cells. *J. Phys. Chem. Lett.* **6,** 3808–3814 (2015).
40. Belisle, R. A. *et al.* Interpretation of inverted photocurrent transients in organic lead halide perovskite solar cells: proof of the field screening by mobile ions and determination of the space charge layer widths. *Energy Environ. Sci.* **131,** 6050 (2017).
41. Snaith, H. J. *et al.* Anomalous hysteresis in perovskite solar cells. *J. Phys. Chem. Lett.* **5,** 1511–1515 (2014).
42. Li, W. *et al.* Enhanced UV-light Stability of Planar Heterojunction Perovskite Solar Cells with Caesium Bromide Interface Modification. *Energy Environ. Sci.* **9,** 490–498 (2016).
43. Shao, Y., Xiao, Z., Bi, C., Yuan, Y. & Huang, J. Origin and elimination of photocurrent hysteresis by fullerene passivation in CH3NH3PbI3 planar heterojunction solar cells. *Nat. Commun.* **5,** 1–7 (2014).
44. Kim, Y. *et al.* Pure Cubic-Phase Hybrid Iodobismuthates AgBi2I7for Thin-Film Photovoltaics. *Angew. Chemie - Int. Ed.* **55,** 9586–9590 (2016).
45. Emrani, A., Vasekar, P. & Westgate, C. R. Effects of sulfurization temperature on CZTS thin film solar cell performances. *Sol. Energy* **98,** 335–340 (2013).
46. Peters, C. H. *et al.* High efficiency polymer solar cells with long operating lifetimes. *Adv. Energy Mater.* **1,** 491–494 (2011).
47. Bush, K. A. *et al.* 23.6%-Efficient Monolithic Perovskite/Silicon Tandem Solar Cells with Improved Stability. *Nat. Energy (under Rev.* 1–7 (2017). doi:10.1038/nenergy.2017.9
48. Azpiroz, J. M., Mosconi, E., Bisquert, J. & De Angelis, F. Defect migration in methylammonium lead iodide and its role in perovskite solar cell operation. *Energy Environ. Sci.* **8,** 2118–2127 (2015).
49. Wang, Q. *et al.* Scaling Behavior of Moisture-induced Grain Degradation in Polycrystalline Hybrid Perovskite Thin Films. *Energy Environ. Sci.* (2017).

doi:10.1039/C6EE02941H
50. Zhang, Y. *et al.* Two-Step Grain-Growth Kinetics of Sub-7 nm SnO2 Nanocrystal under Hydrothermal Condition. *J. Phys. Chem. C* **119,** 19505–19512 (2015).

Acknowledgement

This work was part funded by EPSRC, UK, the European Union Seventh Framework Program under grant agreement number 604032 of the MESO project and AFOSR through project FA9550-15-1-0115. We thank Dr. Amir A. Haghighirad for discussions concerning XRD analysis, Mr. David P. Mcmeekin for discussion concerning device fabrication and film composition analysis. Z.W. would also like to thank Dr. Mattew T. Klug and Ms. Ru Xiang for helping with graph-editing.

Author contributions

H.J.S. and Z. W. conceived of the project. Z.W. designed the experiments, fabricated the devices and thin film samples. Q.L. performed optical spectroscopy and EQE measurements and analysed the data. Z.W. and F.P.C. performed the XRD measurement and analysed the XRD data. N.S. performed SEM measurement and contributed to device fabrication. L.M.H. supervised the optical spectroscopy experiments. H.J.S. supervised the whole project. Z.W. wrote the first draft of the paper. All authors discussed the results and contributed to the writing of the paper.

Additional information

Correspondence and request for materials should be addressed to henry.snaith@physics.ox.ac.uk.

Figure captions

Figure 1. Morphology and crystal phases. a, SEM images of post-annealed perovskite films with different BA concentration, the insets show two-dimensional X-ray diffraction images. The arrows highlight diffraction patterns of the new phases. **b**, Enlarged SEM images.

Figure 2. BA-enhanced 3D perovskite crystalline growth. a, X-ray diffraction rocking curves of the 3D perovskite (200) reflections with varying BA concentrations. The inset shows the FWHM values of the rocking curves. **b**, Pole figure of the (410) reflection of the 3D perovskite phase in the $x = 0.09$ film. RD and TD represent rolling

direction and transverse direction, respectively, within the plane. The [100] direction defines the surface normal direction. **c**, Illustration, depicting the orientation of the 3D perovskite phase in the $x = 0.09$ film, compared to a low-textured $x = 0$ film, showing a preference for [*h*00] direction to align out-of-plane and no orientation preference within the plane. Note that these squares just schematically illustrate the crystal orientation rather than the crystal grains. The real grains impinge together forming dense, pinhole-free morphology as we observed in the SEM images. **d**, Intensity of (100) reflection as a function of time during the perovskite annealing procedure (from room temperature to 175 ^{o}C) for two different BA concentrations ($x = 0$ and 0.09).

Figure 3. 2D-3D perovskite heterostructure. Cross-sectional SEM images of **a**, $FA_{0.83}Cs_{0.17}Pb(I_{0.6}Br_{0.4})_3$ ($x = 0$) film, and **b**, $BA_{0.09}(FA_{0.83}Cs_{0.17})_{0.91}Pb(I_{0.6}Br_{0.4})_3$ ($x = 0.09$) film. **c,** UV-Vis absorption and photoluminescence (PL) spectra. **d**, Time-resolved PL spectra. **e**, Schematic illustration of the proposed self-assembled 2D-3D perovskite film structure and corresponding electronic heterojunction band offsets.

Figure 4. **Device performances of the BA/FA/Cs perovskite solar cells. a**, *J–V* characteristics of optimized perovskite solar cells using $FA_{0.83}Cs_{0.17}Pb(I_{0.6}Br_{0.4})_3$ (labelled as $x = 0$) and $BA_{0.09}(FA_{0.83}Cs_{0.17})_{0.91}Pb(I_{0.6}Br_{0.4})_3$ (labelled as $x = 0.09$) perovskite active layers, measured from forward bias (FB) to short-circuit (SC) and back again. **b,** Stabilised power output (SPO) of the champion cells, determined by holding the cell at a fixed voltage near the maximum power point (MPP) on the *J–V* curve for 60 s, the SPO ratio stands for the ratio between the SPO and *J–V* scanned efficiency. **c**, *J–V* characteristic of a best performing perovskite solar cell using $BA_{0.05}(FA_{0.83}Cs_{0.17})_{0.95}Pb(I_{0.8}Br_{0.2})_3$ active layer, the inset shows the corresponding SPO data. **d**, **e**, Comparison of stability of high-performance non-encapsulated (**d**) and encapsulated (**e**) solar cell devices using $FA_{0.83}Cs_{0.17}Pb(I_{0.6}Br_{0.4})_3$ (labelled as pristine) and $BA_{0.09}(FA_{0.83}Cs_{0.17})_{0.91}Pb(I_{0.6}Br_{0.4})_3$ (labelled as BA/FA/Cs) perovskite active layers. The devices are aged under xenon lamp simulated full spectrum AM1.5, 76 mW cm^{-2} equivalent irradiance in air without any UV filter, held at open-circuit during aging, and tested at different time intervals under a separate AM1.5 100mW cm^{-2} solar simulator. The Suntest XLS+ aging box irradiates pulsed light. There is an early burn-in with an exponential decay over the first ~100 h followed by an approximate linear decay. The light grey and red lines in (**d**) and (**e**) display the actual efficiency decay of eight pristine devices and eight BA/FA/Cs devices, respectively. The navy blue and red lines show the averaged device efficiency decays. The time to 80% of the post burn-in decay (t_{80}) of

champion devices is shown on the graph (with the t_0 efficiency extrapolated back to the y-axis from the linear fit, as shown in **Fig. S12 and S13**). The cell structure is glass/FTO/SnO_2/fullerene/perovskite/spiro-OMeTAD (with Li-TFSI and tBP additives)/Au. We note that PCBM is employed as the n-type fullerene for the devices in (**a**), (**b**) and (**c**), and C_{60} in the devices reported in (**d**) and (**e**).

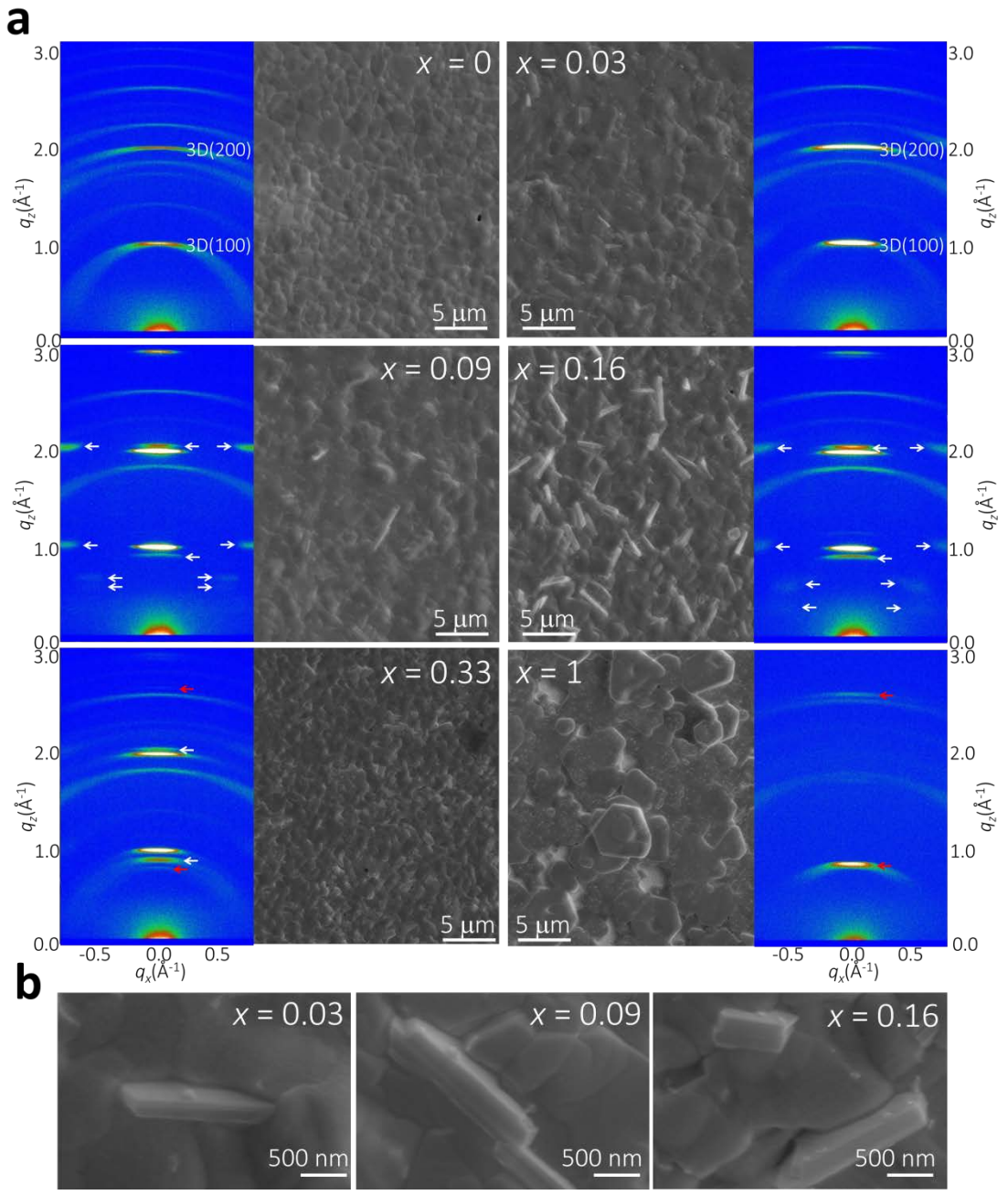
a
x = 0
x = 0.03
x = 0.09
x = 0.16
x = 0.33
x = 1
3D(200)
3D(100)
5 μm
q_z(Å^{-1})
q_x(Å^{-1})
b
x = 0.03
x = 0.09
x = 0.16
500 nm

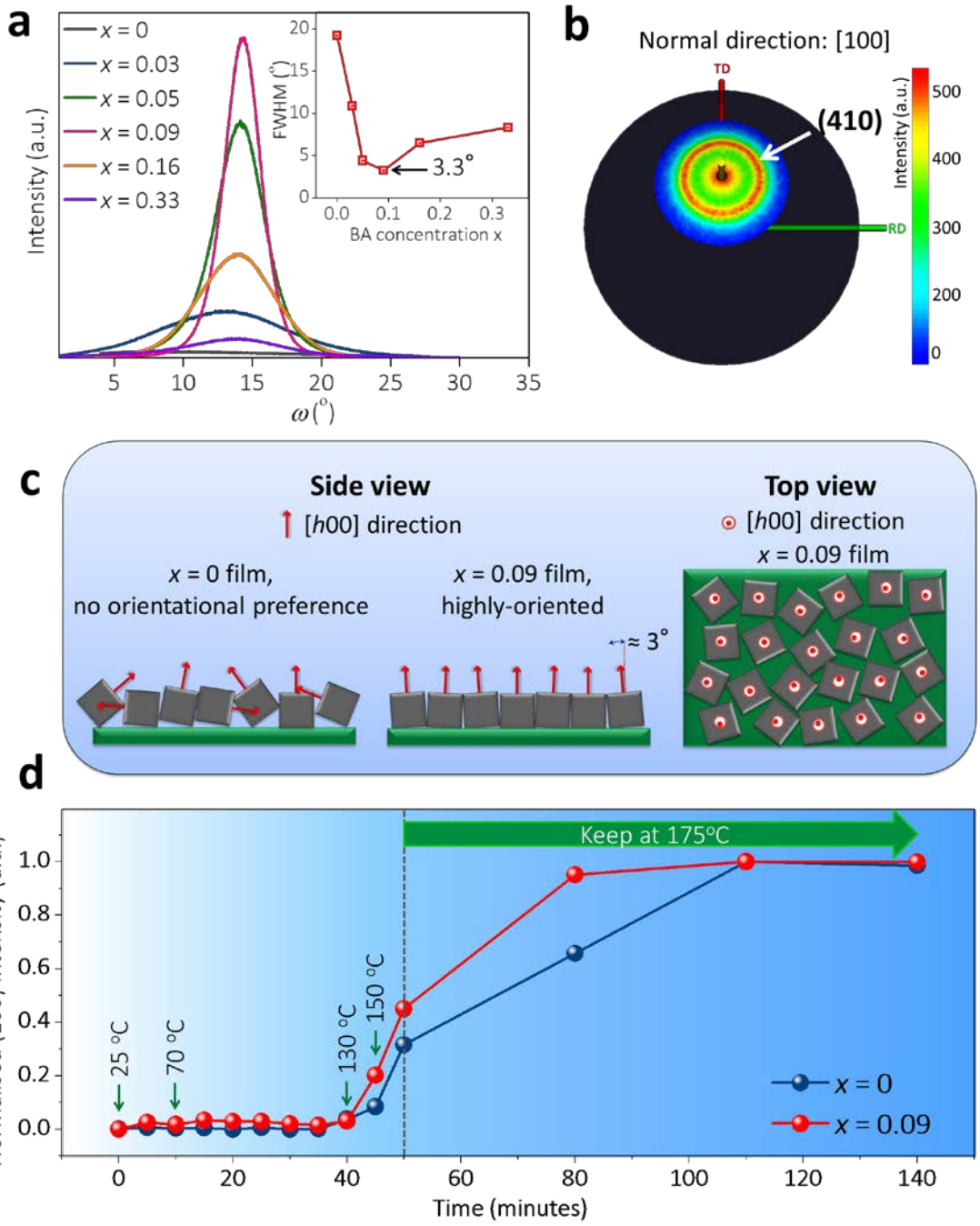
a
x = 0
x = 0.03
x = 0.05
x = 0.09
x = 0.16
x = 0.33
Intensity (a.u.)
ω(°)
FWHM (°)
3.3°
BA concentration x
b
Normal direction: [100]
TD
RD
(410)
Intensity (a.u.)
c
Side view
[h00] direction
x = 0 film,
no orientational preference
x = 0.09 film,
highly-oriented
≈ 3°
Top view
[h00] direction
x = 0.09 film
d
Keep at 175°C
25 °C
70 °C
130 °C
150 °C
Normalised (100) intensity (a.u.)
Time (minutes)
x = 0
x = 0.09

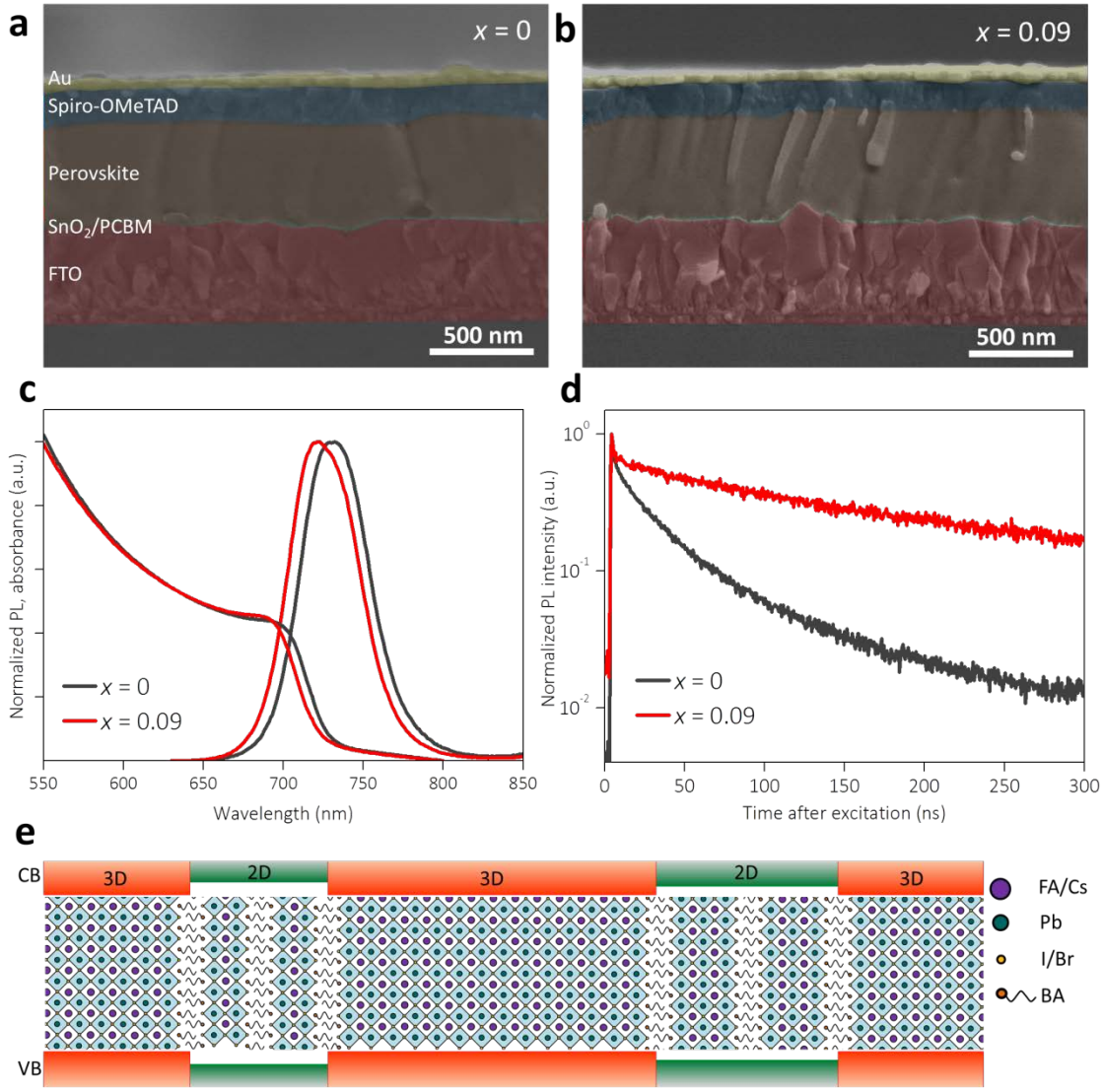
a
x = 0
Au
Spiro-OMeTAD
Perovskite
SnO2/PCBM
FTO
500 nm
b
x = 0.09
500 nm
c
Normalized PL, absorbance (a.u.)
x = 0
x = 0.09
550
600
650
700
750
800
850
Wavelength (nm)
d
Normalized PL intensity (a.u.)
10^0
10^-1
10^-2
x = 0
x = 0.09
0
50
100
150
200
250
300
Time after excitation (ns)
e
CB
3D
2D
3D
2D
3D
VB
FA/Cs
Pb
I/Br
BA

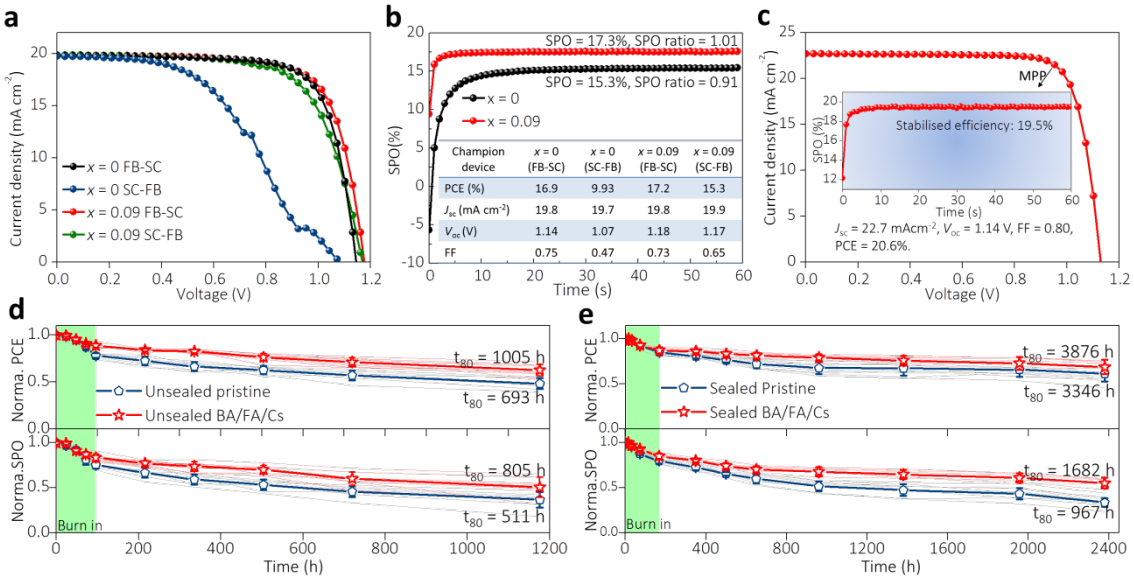
a
Current density (mA cm^{-2})
Voltage (V)
x = 0 FB-SC
x = 0 SC-FB
x = 0.09 FB-SC
x = 0.09 SC-FB
b
SPO (%)
Time (s)
SPO = 17.3%, SPO ratio = 1.01
SPO = 15.3%, SPO ratio = 0.91
x = 0
x = 0.09
Champion device | x = 0 (FB-SC) | x = 0 (SC-FB) | x = 0.09 (FB-SC) | x = 0.09 (SC-FB)
PCE (%) | 16.9 | 9.93 | 17.2 | 15.3
J_{sc} (mA cm^{-2}) | 19.8 | 19.7 | 19.8 | 19.9
V_{oc} (V) | 1.14 | 1.07 | 1.18 | 1.17
FF | 0.75 | 0.47 | 0.73 | 0.65
c
Current density (mA cm^{-2})
Voltage (V)
MPP
SPO (%)
Time (s)
Stabilised efficiency: 19.5%
J_{sc} = 22.7 mAcm^{-2}, V_{OC} = 1.14 V, FF = 0.80,
PCE = 20.6%.
d
Norma. PCE
Norma.SPO
Unsealed pristine
Unsealed BA/FA/Cs
t_{80} = 1005 h
t_{80} = 693 h
t_{80} = 805 h
t_{80} = 511 h
Burn in
Time (h)
e
Norma. PCE
Norma.SPO
Sealed Pristine
Sealed BA/FA/Cs
t_{80} = 3876 h
t_{80} = 3346 h
t_{80} = 1682 h
t_{80} = 967 h
Burn in
Time (h)